Photometric Redshift Estimation of Strongly Lensed Galaxies

THESIS

submitted in partial fulfillment of the
requirements for the degree of

MASTER OF SCIENCE

in

ASTRONOMY AND COSMOLOGY

Author :   Danial Rangavar Langeroodi
Student ID :   2238241
Supervisor :   Prof. Henk Hoekstra
2nd supervisor :   Dr. Alessandro Sonennfeld
2nd grader :   Prof. Rychard Bouwens

Leiden, The Netherlands, July 31, 2019

Photometric Redshift Estimation of Strongly Lensed Galaxies

Danial Rangavar Langeroodi

Leiden Observatory, Leiden University
P.O. Box 9500, 2300 RA Leiden, The Netherlands

July 31, 2019

Abstract

Studying the strong gravitational lensing by massive early-type de-flectors, to estimate the mass inside the Einstein Radius of such galax-ies, requires measuring the source redshift; it is expensive to detect the emission lines of the typically faint source, and due to the photometry complications raising from the lens surface brightness, photometric red-shift (photo-z) has always been unreliable. Fitting elliptical light profiles to the surface brightness of the source and deflector, can be a candidate to handle the aforementioned complications; the accuracy of photo-z es-timations, implementing this method will be tested on a simulated test sample. Surface brightness of the source was reproduced, using ellipti-cal isophotes, and a spectral energy distribution (SED), chosen from the empirical/population synthesis templates with $z \in (1,3)$. This source was added on top of a massive early-type lens, obtained from the wide layer *grizy* photometry of Hyper Supreme-Cam, within 2″ angular separation. Using this method, for a sample of 100 simulated system, source mag-nitudes were measured in *grizy* bands, with *i*-band standard deviation $\sigma(\Delta m_i / m_i) = 0.10$; the goodness of the fit depends on surface brightness ratios, lens light model shape, and contamination light of the other galax-ies. Based on these magnitude measurements, reliable photo-z(s) were achieved with $\sigma(\Delta z / 1 + z_{phot}) = 0.08$, and 13.9% outlier fraction. These results, despite the need to getting verified on more realistic samples, val-idates this technique as an accurate/extremely economical tool for strong lensing studies.

Contents

Chapter 1

Introduction

The standard-spatially flat ΛCDM cosmology is consistent with the cosmic microwave background anisotropy measurements (Planck Collaboration et al., 2018a,b), and successfully reproduces the observed large scale structure of the universe (Komatsu et al., 2009; Navarro et al., 1996; Planck Collaboration et al., 2018b). Galaxy formation as a result of gas condensation in the potential wells of gravitationally collapsed cold dark matter over-densities (dark halos), is a picture, mutually agreed upon, by theory, observations, and simulations (Cole et al., 2000; Davis et al., 1985; Hernquist, 1990; Komatsu et al., 2011; Peebles, 1980; Planck Collaboration et al., 2018b; Schaye et al., 2015; White & Rees, 1978).

Significant progress in dark matter detection has been made by measuring the total mass of the nearby galaxies via kinematics of mass tracers (e.g. Bertin & Stiavelli, 1993); the total mass being higher than the stellar mass for such cases confirms the necessity of dark matter to describe galaxy dynamics. Estimation of galactic dark matter fraction is of extreme importance in studies of baryon contraction efficiency within the dark matter, their effect on the dark matter distribution, and consequently, insights on cooling and heating processes contributing to the galaxy formation (Cole et al., 2000). In order to constrain the dark matter mass profile, or even simpler, dark matter fraction of a galaxy, we need to constrain the baryonic mass, which is related to the luminosity of the galaxy by Stellar Initial Mass Function (IMF). Observational evidence and simulations support the domination of baryons close to the galaxy center, and dark matter at large radii, with numerical simulations predicting $\rho_{DM} \propto 1/r$ (e.g. Navarro et al., 1997). However, dark matter studies of early-type galaxies face two main challenges; paucity of their mass tracers, and our poor understanding of their IMF (Treu, 2010). For local galaxies IMF has been

1

determined by studying the stars individually, which is not possible for higher redshifts; there has been assumptions about IMF being global, and extending the application of local IMF determinations (for example that of Salpeter, 1955) to higher redshifts, which would not necessarily hold true if it depends on redshift (see Sonnenfeld et al., 2013).

Gravitational lensing can be used as an alternative to galaxy dynamics for higher redshift mass measurement. Matter, curving the geometry of space-time, causes the light to deflect, and as an extreme case, strong gravitational lensing happens when the angular separation of the source and deflector is very small $\sim 1''$. Since strong lensing observables, including relative positions, flux ratios, and time delays between multiple images, depend on the gravitational potential of the deflector and its derivatives (Treu, 2010), it can be used to estimate the mass of the deflector (Sonnenfeld et al., 2013), and cosmological parameters (Collett & Auger, 2014; Suyu et al., 2014); this would provide us with useful constraints on IMF (Sonnenfeld et al., 2012), and dark matter fraction (Auger et al., 2010; Barnabè et al., 2011; Treu, 2010). Other features, such as extreme magnification, can be used for observation of faint objects (e.g. AGNs, high redshift galaxies) (Treu, 2010).

Nevertheless, for a detected strongly lensed system, without knowing the redshift of the source and deflector, it would not be possible to infer the mass information. Since the strong lensing cross section increases with source redshift (Meneghetti et al., 2003), the source is faint in general, hence, emission lines become extremely hard to detect, and as a result, spectroscopy requires long exposure times without guaranteed success (tens of minutes on best ground based telescopes, (see Ruff et al., 2011)). Therefore spectroscopic redshifts are scarcely available for sources, and obtaining it would be too expensive.

Photometric redshift estimation (photo-z) is an alternative tool for redshift measurement, in which instead of identifying the emission lines, redshift is calculated by fitting the empirical, or population synthesis Spectral Energy Distributions (SED), to the observed spectra in multiple broad photometry bands (e.g. Benítez, 2000; Tanaka et al., 2018), which is based on assuming the SED to depend on redshift. Photometry on large galaxy surveys have achieved redshifts with standard deviations of under 0.05, and outlier fractions smaller than 10% (e.g. Tanaka et al., 2018). The goodness of the photo-z fit depends on how good the flux in each band can be measured; for a strongly lensed system, due to the small angular separation, and the typical brighter deflector, source photometry will get complicated due to the surface brightness of the lens (Treu, 2010); this makes it hard to implement photometric redshift estimators in practice.

In order to perform a reliable photometric estimation for the source, it is essential to handle these complications; one practical way would be fitting light models to the surface brightness of the source and deflector, using the best fit to measure the flux of source and lens in each photometry band, and estimate the redshift based on the measured fluxes. Here, the accuracy of this method will be tested on a simulated test sample, produced by adding a simulated source ($z \in (1,3)$), having elliptical isophotes, with the flux of each band chosen from the SED template libraries (those of Benítez, 2000), on top of a massive early-type galaxy selected from Sonnenfeld et al. (2019), having spheroidal morphology. Moreover, the accuracy dependence of photometric measurements on characteristics of the system, including surface brightness ratios, shape of the lens surface brightness, and contaminating galaxies close to the system, will be investigated.

Because of the small cross-section (Meneghetti et al., 2003), limited angular resolution of our surveys (affecting the image-based searches), and, faint sources without emission line detection (minimizing the efficiency of spectroscopy based selection methods), strong lensing is a rarely detected phenomenon, with restricted applications (Treu, 2010); combining the results of SLACS (Bolton et al., 2006), CLASS, SQLS (Inada et al., 2012), SL2S (Cabanac et al., 2007), and BELL (Brownstein et al., 2012), alongside Kilo-Degree Survey (KIDS, Kuijken et al., 2015)[*], Hyper Supreme-Cam (HSC, Aihara et al., 2018)[†], and the Dark Energy Survey (DES, Diehl et al., 2017), results a total number of 600 strong lenses. Fortunately, the upcoming wide and deep sky surveys such as as Euclid (Laureijs et al., 2011) and Large Synoptic Survey Telescope (Ivezić et al., 2019), with improved depth, area, and resolution, and equipped with more advance selection algorithms (e.g. Brault & Gavazzi, 2015; Gavazzi et al., 2014), will increase the population of the galaxy scale lens sample by orders of magnitude (Collett, 2015; Kuhlen et al., 2004).

Reliable lens modeling for each strongly lensed is a long process, requiring constant human interpretation (Treu, 2010). Due to the large number of strongly lensed galaxies, about to become available, there is a raising sense of urgency in the community, to develop faster/more efficient ways to extract the information from such objects, since it would not be possible to study all of them individually. This will also be addressed throughout this paper, investigating the possibility of developing an algorithm capable of estimating the photometric redshifts for a strongly lensed system,

---

[*]http://kids.strw.leidenuniv.nl

[†]https://hsc-release.mtk.nao.ac.jp

with minimal human intervention.

Chapter 2, provides a brief introduction to strong gravitational lensing and its applications for mass measurement. Chapter 3 will be an introduction to photometric redshift estimation algorithms, in which, a suitable photo-z estimator will be selected and tested for future implementation throughout the paper. Chapter 4 will go through the process of fitting surface brightness profiles to the source and deflectors; the parameters involved in the goodness of the light model fits will be investigated. In chapter 5 I will test the algorithm developed through chapters 3 and 4, and finally will discuss the results and summarize them in chapters 6, and 7.

Chapter 2

Gravitational Lensing

Coupling of mass and space-time geometry, explained by General Relativity, causes the space-time curvature around matter, which will change the light trajectories; the deflection of the source light, along its way to the observer, by massive objects (deflectors), and the resulting consequences are referred to as Gravitational Lensing. Although deriving the deflection angle in curved space-time requires solving the complete set of general relativistic field equations, which is a complicated task, the simplicity of gravitational lensing allows for various simplifying assumptions (Narayan & Bartelmann (1996), and 2006 Saas Fee lectures for a complete treatment and application of (strong) gravitational lensing).

2.1 Lensing Basics

Almost all the light deflection happens in a very short distance from the the deflector, therefore, the lens mass can be replaced by its two dimensional projection on the deflector plane, perpendicular to the line of sight, with a surface mass density Σ,

$$\Sigma(\vec{\xi}, z) = \int \rho(\vec{\xi}, z) dz, \tag{2.1}$$

where z is along the line of sight, and $\vec{\xi}$ is the two dimensional vector in the lens plane; this is called thin lens approximation. The Deflection Angle $\vec{\hat{\alpha}}$ is related to Σ via,

$$\vec{\hat{\alpha}}(\vec{\xi}) = \frac{4G}{c^2} \int \frac{(\vec{\xi} - \vec{\xi}')\Sigma(\vec{\xi}')}{|\vec{\xi} - \vec{\xi}'|^2} d^2\xi'. \tag{2.2}$$
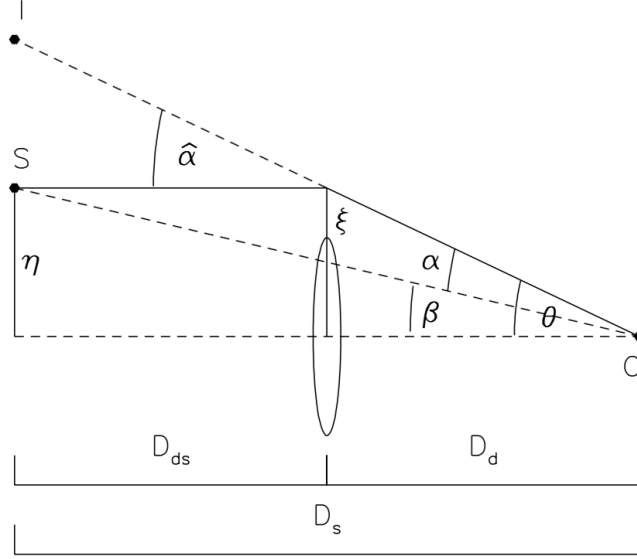
5

Figure 2.1: *sketch of the lensing phenomenon, S is the source and O is the observer. I is imaginary position of the lensed image, $\hat{\alpha}$ the deflection angle, and α the reduced deflection angle; β, θ have also been specified in the figure. ξ is the vector on lens mass plane, D_d is the angular diameter distance of the lens from the observer, D_s source from the observer, and D_{ds} source from lens (Narayan & Bartelmann, 1996).*

Figure 2.1 shows the lensing phenomenon for an observer located at O, with angular diameter distances D_d (lens from observer), D_s (source from observer), and D_{ds} (lens from source). Defining the dimensionless Reduced Deflection Angle $\vec{\alpha}$ as,

$$\vec{\alpha} = \frac{D_{ds}}{D_s}\vec{\hat{\alpha}}, \tag{2.3}$$

from figure 2.1, it can be showed,

$$\vec{\theta} D_s = \vec{\beta} D_s + \vec{\hat{\alpha}} D_s \rightarrow \vec{\beta} = \vec{\theta} - \alpha(\vec{\theta}), \tag{2.4}$$

called the Lens Equation. This is a nonlinear equation, which means it has multiple solutions for θ, and therefore, it can be possible to detect more than one image corresponding to a single source.

Equation 2.2 can be simplified further by assuming a circularly sym-

metric lens;

$$\vec{\alpha}(\vec{\xi}) = \frac{4GM(\vec{\xi})}{c^2\vec{\xi}} \tag{2.5}$$

in which $M(\vec{\xi})$ is the mass enclosed in radius ξ. Inserting this deflection angle in lens equation (eq. 2.4), and replacing θ with ξ/D_d, results,

$$\vec{\beta} = \vec{\theta} - \frac{D_{ds}}{D_d D_s} \frac{4GM(\vec{\theta})}{c^2\vec{\theta}} = \vec{\theta} - \vec{\alpha}(\theta). \tag{2.6}$$

Setting $\beta = 0$ (assuming the source being exactly behind the lens on the optical axis) in equation 2.6, and having non-trivial solution for θ, source will be imaged as a ring around the lens, called Einstein Ring, with a corresponding radius, called Einstein Radius θ_E,

$$\theta_E = \left[\frac{4GM}{c^2} \frac{D_{ds}}{D_d D_s}\right]^{1/2}. \tag{2.7}$$

The critical surface mass density Σ_{crit} is defined by demanding the lens equation having a non-trivial solution for $\beta = 0$, resulting the Einstein Ring; defining the mean surface mass density as $\bar{\Sigma} = M(\xi)/(\pi\xi^2)$,

$$\Sigma_{crit} = \bar{\Sigma} = \frac{c^2}{4\pi G} \frac{D_s}{D_d D_{ds}}. \tag{2.8}$$

If the surface mass density of the lens is above this critical density, it can generate multiple source images. Due to circular symmetries, if the source is exactly on the optical axis ($\beta = 0$) of an axisymmetric lens, it will be imaged as a ring, called the Einstein Ring (Kuijken, 2003; Narayan & Bartelmann, 1996).

2.2 Strong Gravitational Lensing Observables

If the source is close to the optical axis of a massive lens, strong lensing, with high magnification, and multiple source images, will happen. Galaxy-galaxy strong lensing generates multiple source images around the Einstein Radius, which can be used to measure Einstein Radius, and consequently approximating the enclosed mass inside it $M(\theta_E)$. For example, assuming the mean density inside Einstein Radius being equal to critical density Σ_{crit}, one can write,

$$M(\theta_E) = \pi R_E^2 \Sigma_{crit} = \pi(D_d\theta_E)^2 \Sigma_{crit}. \tag{2.9}$$

Which is the most simple approximation to the problem, and in practice constraining the mass profile for the deflector is needed; for example by fitting singular isothermal ellipsoids (SIE) to the lens image (Kassiola & Kovner, 1993; Kormann et al., 1994).

Einstein Radius for early-type galaxies can be estimated with high accuracy; for example Bolton et al. (2008), studying 63 clear strongly lensed candidates of the SLACS survey, with lenses having early-type morphology, by using a singular isothermal sphere model for the deflector mass, estimated the Einstein Radius of the deflectors with 2% accuracy. Knowing the redshift of the lens, Einstein Radius can be converted to the Effective Radius $R_E = D_d \theta_E$, which, in addition to the critical density, can be used to estimate the mass inside the Einstein Radius. The critical density is a function of the source and deflector redshifts (equation 2.8), hence, in order to estimate the mass inside the Einstein Radius for a deflector of a strongly lensed system, source and lens redshifts must be available. Typically, lens redshifts are already known, or achievable through spectroscopy, but, as mentioned before (and will be discussed further in chapter 3), that is not be the case for source galaxies.

As discussed in the introduction, photometric redshift estimation can be an alternative method for estimating the source redshift. However, Einstein Radius for massive early-type galaxies is typically around $1''$ (Bolton et al., 2008); this small angular separation between the source and deflector, complicates the source surface brightness, and consequently its photometry. Chapter 4 will provide a practical approach to handle the photometry complications, by fitting elliptical light models to the source and deflector.

Photometric Redshift Estimation

Spectroscopic redshift estimation is the most reliable method for measuring galaxy redshifts; by identifying absorption/emission lines in the galaxy spectrum, redshift is measured by comparing the observed and rest frame wavelengths. For faint objects, since emission lines become harder to detect, spectroscopy will get more expensive, requiring longer exposure times; this will be especially the case for the sources of strongly lensed systems. As an example, Ruff et al. (2011) attempted spectroscopy for a sample of 17 strongly lensing systems, and with an exposure time of 40 minute on average over almost 4 years, between 2006 to 2011, using Low Resolution Imaging Spectograph (LRIS) on the Keck I, achieved deflector redshifts for all the 17 cases, and only 6 source redshifts. Moreover, when dealing with a large galaxy survey, time wise, it will not be possible to perform spectroscopy for all the objects; upcoming results of deep sky, galaxy imaging surveys, such as Euclid (Laureijs et al., 2011) and Large Synoptic Survey Telescope (Ivezić et al., 2019), with large number of deep/faint galaxies, would raise the issue further. In such scenarios, when the object is faint, or there are simply too many objects to attempt spectroscopy for all of them, photometric redshift estimation (photo-z from now on) by providing a faster, but, less reliable, redshift measurements, which does not rely on detection of line emissions, has proven to be of use; for example Tanaka et al. (2018), using photometric methods (to be described in this chapter), achieved $\sigma(\Delta z/1 + z_{phot}) \sim 0.05$ and an outlier fraction of 15%, for galaxies down to base band photometry band magnitude of 25 from the HSC survey (Aihara et al., 2018). There are many photo-z algorithms available, but they can be categorized as Template Fitting (SED Fitting) (e.g. BPZ (Benítez, 2000), hyperZ (Bolzonella et al., 2000), and (Tanaka et al., 2018)), and Training Sets (Machine Learning, e.g. Aihara et al., 2018;

9

Connolly et al., 1995; Koo, 1985). A template fitting algorithm will be employed throughout this paper.

3.1 Template Fitting

In photo-z methods, instead of identifying the spectral lines in the spectrum, flux of the distant object is measured in multiple photometry bands (i.e. colors), covering a broad range of wavelength; redshift is estimated by assuming the existence of a relation between colors and redshift. In Machine Learning techniques, by using an empirical subset of the galaxies under study (for which the spectroscopic redshifts are available), a $z = z(C, m_0)$ function is derived by using colors and magnitudes of the respective subset; this function is used to predict the redshift of rest of the galaxies. The main challenge is that whenever the spectroscopic redshift is not available for the regions under study, it would not be possible to derive the redshift-color function, hence making it impossible to measure photo-z in such regions (e.g. Carrasco Kind & Brunner, 2013; Connolly et al., 1995).

In Template Fitting (SED Fitting) method, the observed Spectral Energy Distribution (SED) is fitted by using a library of previously generated templates. The color c of the photometry band b is defined as $c_b = f_b / f_0$, in which f_b is the flux in b-band and f_0 the base-band flux; templates are produced via known galaxy spectra and redshifts, provided by previous spectroscopic observations, or generated with population synthesis (e.g. Bruzual & Charlot, 2003; Coleman et al., 1980). Each template consists of $C = C(z, T_n)$ points (where $C = \{c_\alpha\}$ - with α referring to the filter $\in (1, m)$); including various templates, covering different galaxy morphological types, a $C = C(z, T_n)$ library is produced.

Magnitude can be derived from the photometry flux; given the observed set of magnitudes $M = \{m^{obs}\}$ with the multi-band photometry, $P(z|\{m^{obs}\})$, the probability of redshift being z is given by,

$$P(z|\{m^{obs}\}) = \int P(z, C|\{m^{obs}\}) dC \qquad (3.1)$$

for which the integral is calculated over the $C(z, T_n)$ libraries. This method, attempting to fit the templates to the observed colors, inherits a problems; namely, template incompleteness (Benítez, 2000). Briefly described, template incompleteness happens when there is no nearby point in the $C(z, T_n)$ space, corresponding to the observed colors. When simulating the test sample (section 4.1), source spectrum will be selected from the

SED template library, hence, this problem can be ignored when estimating the source redshift throughout this paper.

3.2 Template Fitting Algorithm

In this section, a simple template fitting algorithm is going to be developed, which, for each flux set (multi-band photometry of a single galaxy, $F = \{f^{obs}\}$, or equivalently $M = \{m^{obs}\}$), returns a highest probability redshift, and a redshift probability distribution function (PDF). Given a set of multi-band photometric measurement for each galaxy, each redshift z in a given redshift range (e.g 1.0 to 5.0) will be assigned a value $p(z|\{m^{obs}\})$ according to equation 3.1, stating the probability of the true redshift being equal to z, given the observed set of magnitude measurements M for the galaxy. Assuming flat priors, i.e. $P(C, z)$= constant, calculating $p(z|\{m^{obs}\})$ is the same as measuring likelihood (or equivalently χ^2), for each z in an arbitrary redshift range (when searching for the true redshift, this range should include that redshift as well), which results the PDF of redshift for the given range.

As mentioned in section 3.1, the integration of equation 3.1 is calculated over the whole template library. Similar templates to those of Benítez (2000) and Sawicki et al. (1997) will be used as the template library here, including the four population synthesis E/S0, Sbc, Scd, and Irr morphological types of Coleman et al. (1980), and the two star-bursting galaxies of Kinney et al. (1996). To include the UV region, all of these template have been extrapolated with a cutoff at 912 $\overset{\circ}{A}$, and then corrected for intergalactic absorption using the methods of Madau (1995). The T_n value goes through the aforementioned template library, with arbitrary normalization.

Magnitude measurements always carry some uncertainty, if the observed magnitudes $\{m^{obs}\}$ follow a Gaussian distribution function around the true magnitude, likelihood can be written as,

$$p(z, T_n, b|\{m_\alpha^{\text{observed}}\}) \propto \frac{\chi^2(z, T_n, b)}{2} = \sum_\alpha \frac{(m_\alpha^{\text{observed}} - m_\alpha^{\text{template}})^2}{2\sigma_{m_\alpha^{\text{observed}}}^2} \quad (3.2)$$

in which the sum is over the photometry filters, $\sigma_{m_\alpha^{\text{observed}}}$ is the uncertainty of the observed magnitude in filter α, and $m_\alpha^{\text{template}}$ is related to the tem-

plate fluxes via,

$$m_\alpha^{\text{template}} = -2.5 \log(b f_\alpha^{\text{template}}) \tag{3.3}$$

for which b is again the normalization constant, being a function of redshift z and template T_n, chosen such that χ^2 is minimized, or in other words,

$$\frac{\partial \chi^2}{\partial b} = 0 \tag{3.4}$$

solving equation 3.4 for χ^2 given by equation 3.2, and inserting $m_\alpha^{\text{template}}$ from equation 3.3 results,

$$\log b = -\left(\sum_\alpha \frac{m^{\text{observed}} - 2.5 \log f_\alpha^{\text{template}}}{\sigma^2_{m_\alpha^{\text{observed}}}} \right) \Big/ \left(2.5 \sum_\alpha \frac{1}{\sigma^2_{m_\alpha^{\text{observed}}}} \right) \tag{3.5}$$

calculating b for each given (z, T_n). Inserting this calculated b in equation 3.3, and hence for $m_\alpha^{\text{template}}$ in equation 3.2, χ^2 for each given set of (z, T_n) can be calculated as well. Marginalization over templates can be done via,

$$p(z|\{m_\alpha^{\text{observed}}\}) \propto \int\limits_{\text{templates}} p(z, T_n, b|\{m_\alpha^{\text{observed}}\})\, dT_n; \tag{3.6}$$

since $b(z, T_n)$ is already fixed by equation 3.5 in order to maximize the probability $p(z, T_n|\{m_\alpha^{\text{obs}}\})$, this is an integration over template space T_n. After marginalizing, there is a probability $p(z|\{m_\alpha^{\text{observed}}\})$ assigned to each redshift in the given redshift range, for a set of multi-band magnitude measurements $M = \{m_\alpha^{\text{observed}}\}$. If the goal is to return a single redshift value as the redshift estimation for the observed multi-band magnitudes, the highest probability redshift can be set equal to the maximum of the $p(z|\{m_\alpha^{\text{observed}}\})$ PDF; but for scientific purposes, people are always interested in the complete PDF.

3.3 Photo-z Dependence on Photometric Uncertainties

It can be seen from equation 3.2, that $p(z, T_n, b|\{m_\alpha^{\text{observed}}\})$ also depends on the magnitude measurement uncertainties $\sigma_{m_\alpha^{\text{observed}}}$, which in turn results $p(z|\{m_\alpha^{\text{observed}}\})$ being a function of uncertainties as well. It is inevitable that by increasing the observation uncertainties, the accuracy of

the photo-z measurements will decrease. To Investigate this, defining the outliers fraction f_{outlier} as,

$$f_{\text{outlier}} = \frac{N(|\Delta z|/1 + z_{phot} > 0.15)}{N_{\text{total}}};$$ (3.7)

in which $N(|\Delta z|/1 + z_{phot} > 0.15)$ is the number of galaxies for which the difference between the (1+photo-z) and (1+true redshift), Δz, is bigger than 15% of the estimated (1+photo-z).

I produced various simulated multi-band magnitude sets $\{m_{n,\alpha}^{\text{observed}}\}$ (α specifying the respective filter, and n simulation number), as follows. Choosing a uniform random number from (1,3) as redshift z, as an approximation to the source redshift of the strongly lensed systems (reasons to become more clear in section 4.1), and a random template point T_n from the templates introduced in section 3.2, results a scale set S, for the five-band photometry,

$$S(z, T) = (\frac{f_g}{f_i}, \frac{f_r}{f_i}, 1, \frac{f_z}{f_i}, \frac{f_y}{f_i}) = (c_g, c_r, c_i, c_z, c_y)$$ (3.8)

in which f is the flux, and the subscript specifying the respective filter. Here i has been chosen as the base photometry band (section 3.1), and the colors of the other bands $C = \{c_\alpha\}$ are calculated respective to this band. By assuming the mean i-band magnitude of the observed galaxies to be 22.0 as a good approximation for the galaxies under study (reasons discussed in section 4.1), I drew a Gaussian random number with 0.5 scatter as the i-band magnitude of the galaxy, m_i. Using the calculated S and knowing m_i, the α-band magnitude m_α would be,

$$m_\alpha = m_i - 2.5 \log c_\alpha.$$ (3.9)

In order to reproduce the observation uncertainties, assuming the uncertainty for each band to follow a Gaussian distribution, simulated magnitudes will be scattered around their true values by adding a Gaussian random realization with zero mean,

$$m_\alpha^{\text{scattered}} = m_\alpha + \mathcal{G}(0, \sigma)$$ (3.10)

σ is the variable that can be changed during the simulations.

I produced simulations with σ varying between 0.01 and 0.20, and used the algorithm developed in section 3.2 to measure the PDF and highest probability redshift for each one of the simulated set of multi-band magnitudes $\{m_\alpha^{\text{scattered}}\}$. To use the template fitting algorithm, assuming
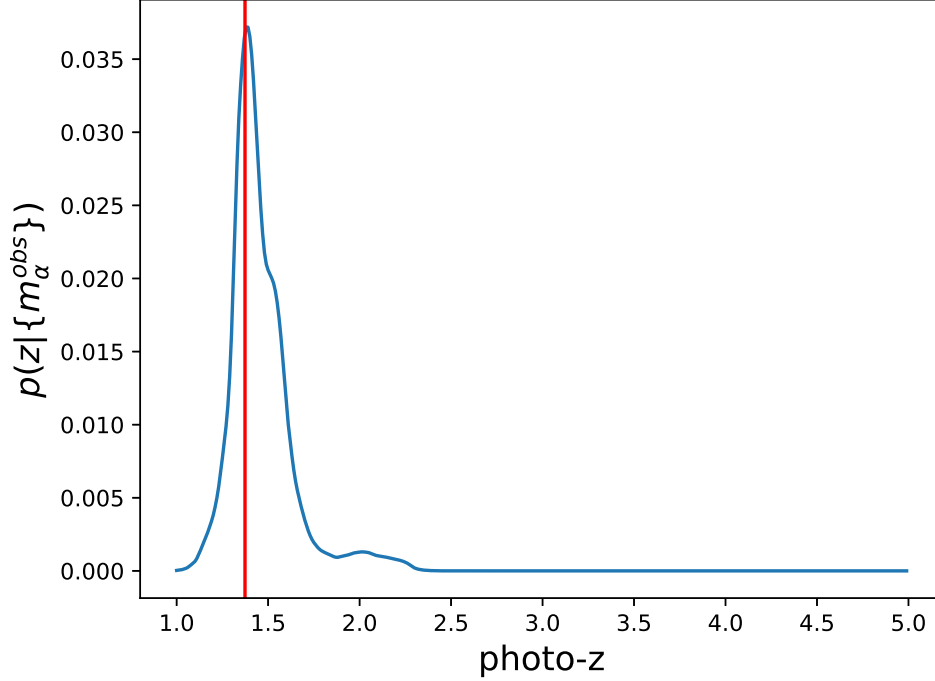
Figure 3.1: *a typical probability distribution function for a simulated SED with* $\sigma = 0.05$ *uncertainty on the 5 grizy band magnitudes, belonging to an Irr galaxy at z = 1.33; this PDF is estimated using the algorithm of this section.*

that observer knows the observation uncertainties, $\sigma_{m_\alpha^{\text{observed}}}$ in equations 3.2, and 3.5, can be set equal to σ of the Gaussian scatter that was used to produce the simulations (equation 3.10). A redshift-template library $S_{\text{library}}(z, T)$, must be produced, to fit the observed magnitudes. Redshift PDF can be calculated using equation 3.6, by marginalizing over all templates; but in practice this integration can not be calculated analytically; hence one needs to settle on a specific redshift resolution to produce the library, which in this section is set to be 0.01 (0.5% for the redshift range of interest - (1,3)). Setting the redshift resolution, $S_{\text{library}}(z, T)$ points will be returned for the selected spectral energy distribution of the library, which in turn would be used to calculate $f_\alpha^{\text{template}}$, and hence $m_\alpha^{\text{template}}$ from equation 3.3. Therefore, given a set $m_\alpha^{\text{observed}} = \{m_\alpha^{\text{scattered}}\}$, normalization constant b, $p(z, T_n, b|\{m_\alpha^{\text{observed}}\})$, and photometric redshift PDF (equations 3.2 to 3.6), can be calculated analytically. Figure 3.1 shows the estimated PDF, on a simulated $\{m_\alpha^{\text{observed}}\}$, belonging to an Irr galaxy at redshift 1.33.

Taking the highest probability redshift as the estimated photo-z, the outlier fraction f_{outlier} can be calculated via equation 3.7; outlier fractions for observation uncertainties (0.01, 0.02, ..., 0.20), have been calculated for 20 samples of 1000 simulated M^{obs}; results can be seen in figure 3.2.
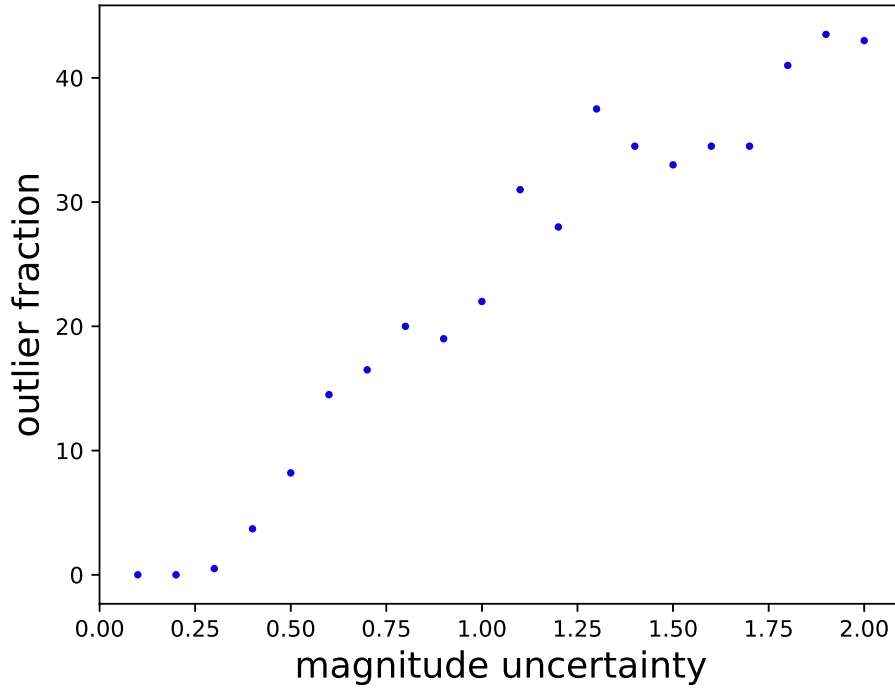

***Figure 3.2:** outlier fractions of the simulated 5-band magnitudes, with varying uncertainty on the magnitude of each band. each point is the result of estimations for 1000 simulated 5-band magnitudes*

It can be seen from the figure 3.2, that for observation uncertainties lower than 0.03, the outlier fraction becomes negligible (under 1%), with standard deviation $\sigma(|\Delta z|/1 + z_{phot}) < 0.01$, which is the resolution of the used redshift templates; the standard deviation for the worst case ($\sigma = 0.2$) is 0.272. As mentioned at the beginning of this section, photometric estimations of Tanaka et al. (2018) resulted an 8% outlier fraction; setting this as a threshold for outlier fractions of the further photometric estimations of this paper, multi-band magnitude measurements with uncertainties below 0.05 will be enough to achieve an outlier fraction better than 8%; standard deviation $\sigma(|\Delta z|/1 + z_{phot})$for such observation uncertainties would be below 0.04.

Chapter 4

Photometric Measurements

One of the main challenges for photometry of strongly lensed systems, is separating the corresponding surface brightness of the source and deflector, which as mentioned before, complicates the multi-band magnitude measurements. As discussed in the previous chapter, photo-z estimations rely on multi-band magnitude measurements, hence, on our understanding of the surface brightness of each object separately. Here, I will suggest a solution, by attempting to describe the surface brightness of each individual object, via an elliptical Sersic light model (Sersic 1968), and combining the individual light models to reproduce the observed image.

Provided that strong lensing conditions are satisfied (chapter 2), multiple distorted source images around the deflector would be observed, complicating the source surface brightness. These effects can all be described by a 2 dimensional Lensing Jacobian (look at Narayan & Bartelmann, 1996, for more details), transforming the source surface brightness to its magnified, distorted version, deflected by the lens mass; the Jacobian can be derived using only lens gravitational potential, and angular diameter distances to the lens and source. Hence, a strongly lensed image can be reduced to a bright deflector, and a projected source at the lensing plane, with a small angular separation in order of $1''$. The transformation from this picture to the strongly lensed version is a simple employment of the Lensing Jacobian, alongside a mass model; using this, to simplify the situation, I will ignore the strong lensing features, namely, shear, convergence, and multiple imagery (and consequently, mass model of the lens), throughout the course of this paper, hence, producing images containing a deflector and a non-lensed source, which will be called Lens-Source Systems from now on.

For real strongly lensed systems, spectroscopic redshift is already avail-

17

able for many of the deflectors, and the real challenge is estimating the source redshift, therefore, in reality, methods of this paper will be most significantly applied on the source; hence, from now on I will focus on source photometry, which will be discussed throughout this chapter, followed by source photo-z estimation in chapter 5.

4.1   Simulations

In this section, I will describe the method used to produce the simulated lens-source systems; the underlying idea would be selecting a massive early-type galaxy as the lens, and adding the image of another higher redshift galaxy as the source on top of it. As a lens sample, I will select a list of galaxies with reliable spectroscopic redshifts, from the wide layer of Hyper Supreme Cam survey (HSC) public data release 1 (PDR1, Aihara et al., 2018)[*], for which spectroscopic redshift, multi-band (g,r,i,z,y) photometry image, point spread function (PSF) of each band, and variance map, are available; selected lenses will be those of Sonnenfeld et al. (2019), drawn from constant-mass (CMASS) sample of the Baryon Oscillation Spectroscopic Survey (BOSS Dawson et al., 2013; Schlegel et al., 2009), visually selected to have spheroidal morphology, with $M_\star/M_\odot > 11.0$, to secure the selection of massive galaxies only; the resulting typical lens redshifts would be 0.5, with mean i-band magnitude of 19.2 and the standard deviation $\sigma = 1.5$.

I will simplify the test sample, by demanding the sources to have elliptical isophotes (for reason which will become clear in section 4.2). Sources are produced, following the approach of chapter 3, with SED drawn from the color-redshift templates by choosing a random redshift in range (1,3), as an approximation to the real source galaxy, and a random value for t_n specifying a random point of the template for a given redshift. Next, since the redshift of the source in a strongly lensed system higher than the lens (source is behind the lens on the line of sight), source magnitudes are bigger than those of lenses (sources are fainter), which is 19.2 in average; hence, by drawing a random number from the Gaussian distribution $\mathcal{G}(22, 0.5)$ for i-band magnitude of the source; respective magnitudes of the remaining bands will be derived knowing their relative flux respective to the *i*-band (which we already know due to SED selection for each source, refer to chapter 3), using equation 3.9.

To reproduce the surface brightness of the source, employing Sersic for-

---

[*]release website: https://hsc-release.mtk.nao.ac.jp

mula (Sersic 1968), an elliptical light model will be produced by selecting random Sersic model parameters and re-scaling the resulting light model with the magnitude of each band, as follows. Radial profile of the surface brightness of a typical galaxy described by a Sersic model, invoking elliptical isophotes, is given by,

$$I(R) = I_e exp\left(- b_n \left[(\frac{R}{R_e})^{1/n} - 1 \right] \right) \tag{4.1}$$

in which R_e is the half light radius, I_e surface brightness at R_e, n the Sersic index, and b_n the normalization constant; R is the geometrical mean, which for an ellipse with semi-major axis a and semi-minor axis b (axis ratio $q = b/a$), is defined as $R = \sqrt{ab}$. It is possible to derive the surface brightness $I(R)$ for a given magnitude,

$$m = -2.5 \log(I_{tot}) + constant \tag{4.2}$$

where the constant is magnitude of zero-point (27.0 here) , and,

$$I_{tot} = 2\pi I_0 R_e^2 [n\Gamma(n)] \tag{4.3}$$

in which I_0 is the maximum surface brightness ($I_0 = eI_e$) (Ciotti & Bertin, 1999). Equations 4.1, 4.3, and 4.2, provided a Sersic Index, half light radius, axis ratio, and magnitude, will produce the whole two dimensional surface brightness of the galaxy. Uniform random numbers for q in (0.3,1.0), and (0.5,3.0) for n, has been drawn; a size-magnitude power-law relation ($\log R_e = -m/5 +$ constant) can be derived using equations 3.9, and 4.3; hence, size can be calculated from the base band magnitude m_i, setting the $\log R_e$ for mean i-band magnitude equal to 3.0 (for R_e measured in pixel space); moreover, a truncated Gaussian scatter was added to the size with $\sigma = 1.0$, with the R_e scattered value being always in range (0,100), in pixel space.

Using each one of the previously derived 5-band magnitudes, with the same random values for $q, R_e,$ and n, 5 scaled versions of the same elliptical light model will be produced. In order to add the simulated source on top of the lens to finalize the lens-source system; I drew random uniform numbers for the squared projected radial distance at the lens plane from the lens center r^2, in units of pixel in range (0,15²); pixel size of HSC is 0.168″, hence with choosing the r in (0,15), the redial separation pf the system will be smaller than 2.5″, as a realistic approximation to the strongly lensed systems; the 2 dimensional position of the source in the lens plane will be completed by drawing a random number for θ (polar coordinates), with (r, θ) = (0,0) being the center of the lens or (50,50) in

pixel space. The only remaining parameter is, the source orientation respective to the x axis, which would be described by drawing a random number in (-90.0,90.0). At the end, for each band, a convolved image of the source with the lens PSF of the same band, is added on top of the lens image (in the mutual band).

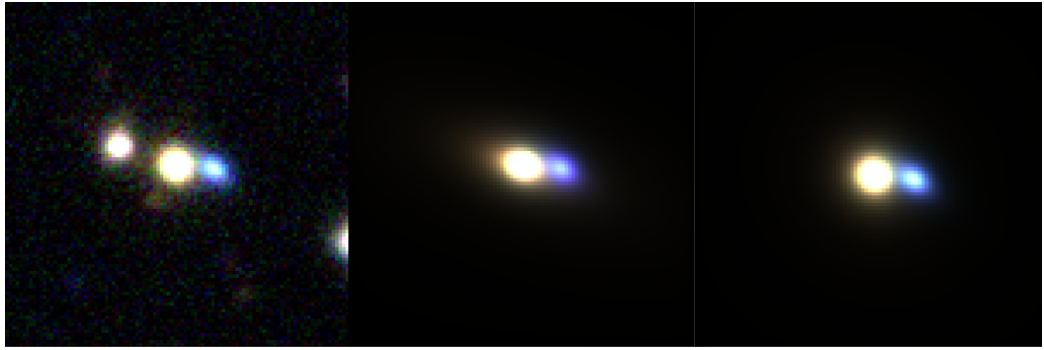## 4.2 Fitting the Light Models to the Simulations

Figure 4.1: *Left: example of a simulated image containing the source (blue galaxy), lens (the center of the image), and an extra galaxy (the red galaxy at the left side of the lens). Middle: respective fit to the simulated image. In order to account for the surface brightness of the extra galaxy, light model fit to the lens is drastically wrong (incorrect orientation parameter pointing to the extra object, and very big major axis (again pointing at the extra object)). Right: respective fit to the simulated image, but this time by using a mask to ignore the surface brightness of the extra galaxy. The fitted light model orientation and major axis are not suffering from the existence of the extra galaxy anymore. These images are the combination of all 5 grizy bands, and and the dimensions are* $16.8''x16.8''$.

Provided simulated images of lens-source systems from the previous section, alongside their respective point spread functions and variance maps, I will start fitting a light model to the surface brightness of each image; the goal is to find multi-band magnitudes of the source as accurate as possible. When fitting the light models to the lens-source systems, I will assume that the positions of the lens and the source are known in pixel space. As discussed in section 4.1, an elliptical surface brightness profile can be reproduced with three parameters, half light radius R_e, axis ratio q, and Sersic index n, using equation 4.1; by choosing starting values for these three parameters, a light model at object position is produced, which then, will be assigned an orientation P_a with respect to the x axis of
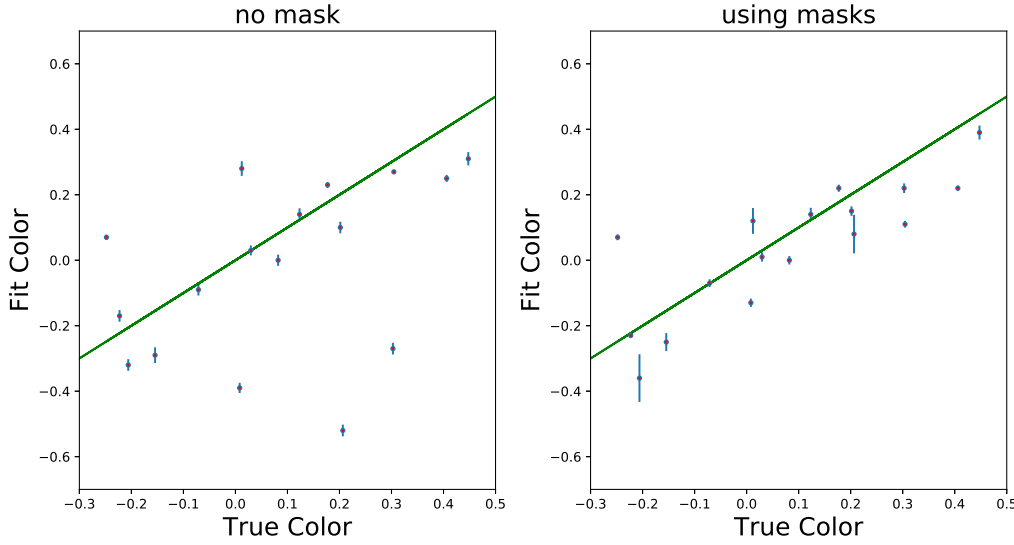
Figure 4.2: *Left: Fitted color ($m_g^{fit} - m_i^{fit}$) vs true color ($m_g^{true} - m_i^{true}$) for 17 simulated lens-source systems; no mask has been used during the fit to ignore the light of contaminating objects (extra galaxies in the image other than the deflector and source). Right: the same 17 simulated lens-sources, fitted using masks to ignore the light of contaminating objects.*

the image. The same elliptical model is then scaled with a guess magnitude for each one of the 5 photometry bands (*grizy*); the combination of $(R_e, n, q, P_a, m_g, m_r, m_i, m_z, m_y)$ at the position of the object, which results the highest likelihood will be returned as the best fit for the object; this combination will be called the light model from now on).

At this stage, I am mainly interested in finding the lens characteristics affecting the goodness of the fit, hence, for the light model fit to the source, the elliptical light model parameters have been limited around their true values as follows; source position within ± 2.5 pixels in each one of the x and y directions, orientation within ± 2.5 degrees, and ± 0.1 for Sersic index, axis ratio, and half light radius.

As mentioned earlier, lens is brighter, and hence, easier to fit, therefore, as a first step, a Sersic light model is fitted to the lens in 5 bands, returning the best fit values; then, by fixing the lens model, which is equal to eliminating the lens model of last step from the lens-source image in every band, another Sersic model for the source is added, which will be fitted to the source at the presence of the fixed lens (on the lens-model eliminated image), returning a best fitted light model for the source in combination with the fitted lens of step one. Last step would be freeing the light model
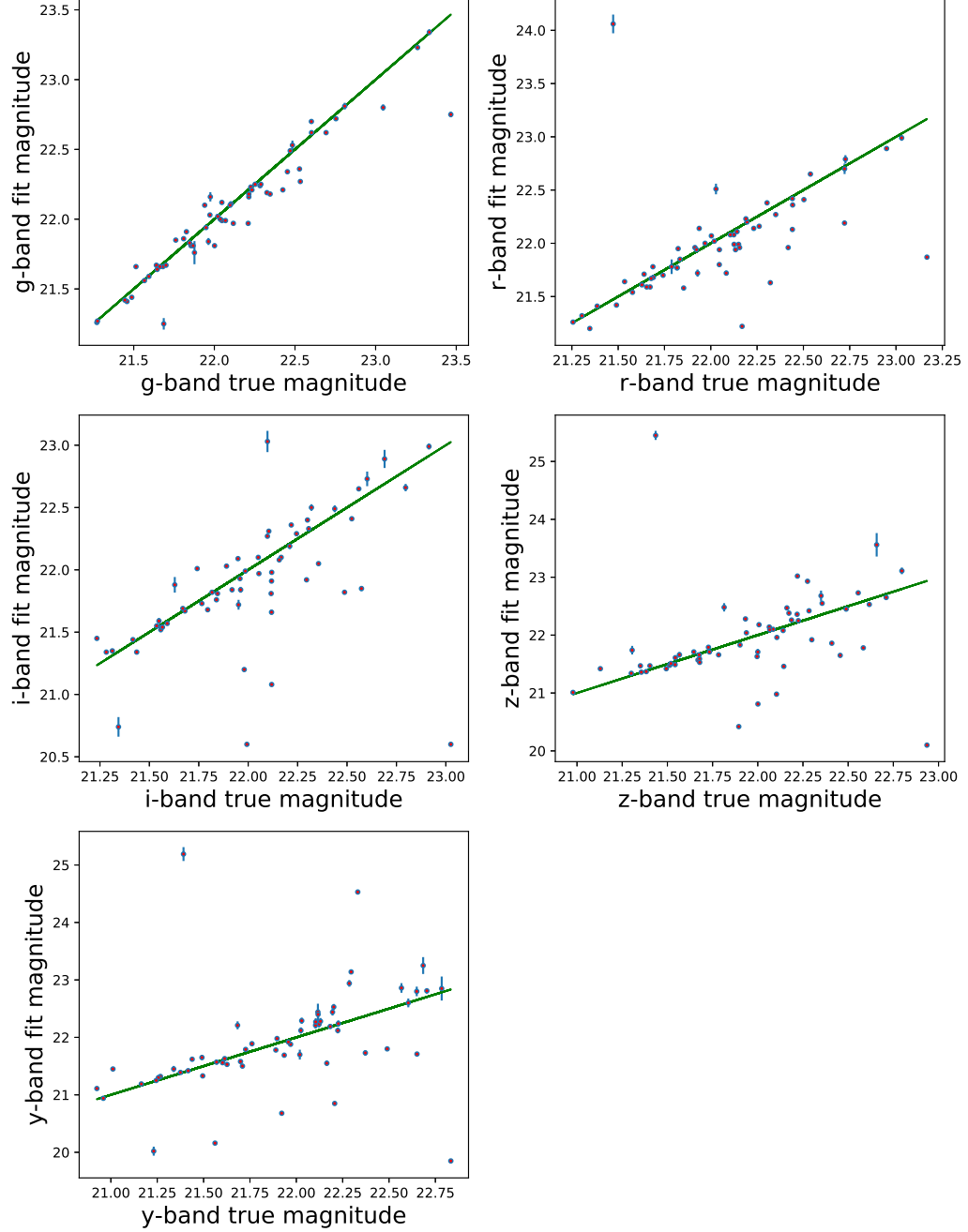
Figure 4.3: *Fitted magnitudes vs true magnitudes, for a sample of 60 simulated lens-source systems, produced following the methods of section 4.1; the surface brightness of extra galaxies (contaminating galaxies) has been ignored through masking. Green line* $m_\alpha^{fit} = m_\alpha^{true}$.
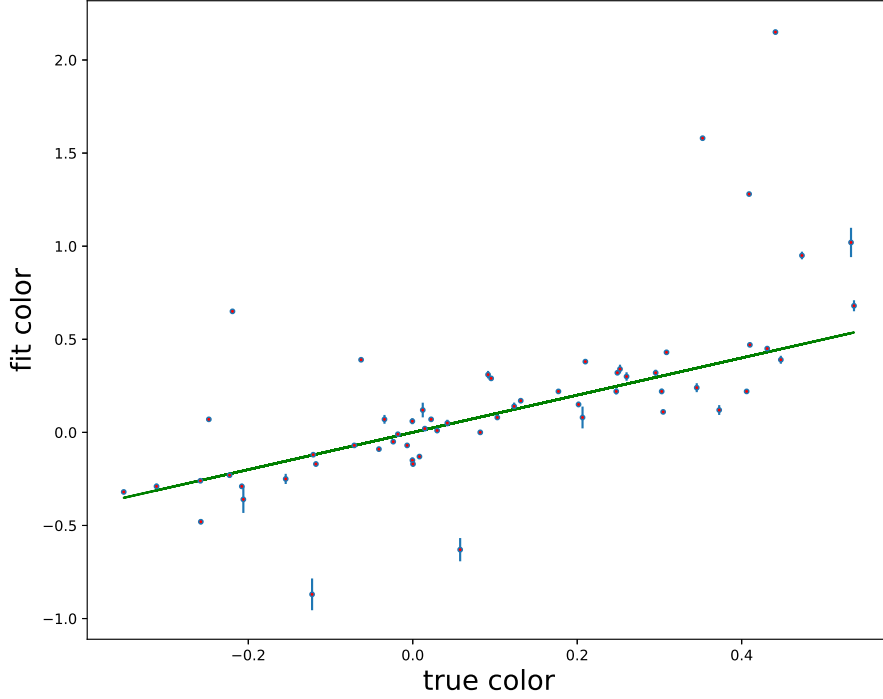
Figure 4.4: *Fitted color vs True color, for a sample of 60 simulated lens-source systems, produced following the methods of section 4.1; the surface brightness of extra galaxies (contaminating galaxies) has been ignored, by masking. Color is defined as the g-band magnitude minus i-band magnitude, and for green line $C^{fit} = C^{true}$.*

of the lens, fitted in first step, and fitting the source and the lens together at the same time, starting from the previously approximated values of steps one and two; at the end, a best fit model, as a combination of two light models fitted at the same time, is returned as the best fit light model for the system.

The Ideal situation would be having an isolated lens-source system to which we want to fit the light models, but that is rarely the case; there are always secondary galaxies other than the lens-source system in the images, complicating the photometry of the lens and source due their contaminating surface brightness. During the fit, the extra light of this extra objects, would be accounted for, by the lens, or source light models, and making the fits less reliable. As an example, figure 4.1 shows a case with a

lens-source system containing an extra galaxy; the light model of the lens, in an attempt to accounting for the light of the extra object, had returned inaccurate fit values, specially for q (the axis ratio of the light model is much higher than what it should be). One way to fix this would be ignoring the contaminating objects, with assigning 0 to the pixel values of the regions where such objects dominate the light; this will be called masking from now on. By implementing the Source Extractor (SExtractor Bertin & Arnouts, 1996), which is a segmentation algorithm that separates the luminous objects in the image and returns the segmented regions, extra objects can be identified and get masked. Using this approach, new masked lens-source image were produced automatically, lacking the galaxies that are not a part of the lens-source system; results of applying a mask can be seen in figure 4.1; q value has been estimated more accurately this time. Figure 4.2 shows a comparison between the goodness of the fits, by comparing the source color estimations ($C^{fit} = m_g^{fit} - m_i^{fit}$), before and after applying the masks, for a sample of 17 simulated images (section 4.1).

After implementing the SExtractor in the fitting algorithm, 60 simulated lens-source systems were produced following the methods of section 4.1, and light models were fitted to the lens and source; results of the comparison between the estimated 5 band (grizy) magnitudes and true magnitudes (used to produce the simulations) can be seen in figures 4.3; the error of magnitude measurements is getting bigger by moving from the g-band, which includes the lowest wavelengths, toward the y-band, which includes the highest wavelength. Since these measured multi-band magnitudes are going to be used to estimate the photometric redshifts, and the goodness of the redshift estimation depends on the relative values of the magnitudes rather than their absolute value (chapter 3), it is useful to use the previously defined a color C^{fit}; figure 4.4 shows the comparison between the estimated color and the true color ($C^{true} = m_g^{true} - m_i^{true}$).

For the test sample of 60 simulated lens-source systems, the standard deviation for each band $\sigma^{\alpha}(\Delta m_{\alpha}^{fit}/m_{\alpha}^{fit})$, with α from (g,r,i,z,y), were calculated to be, $(\sigma^g, \sigma^r, \sigma^i, \sigma^z, \sigma^y) = (0.04, 0.07, 0.10, 0.14, 0.14)$, with color standard deviation $\sigma(\Delta C/C) = 0.07$, $\Delta C = C^{true} - C^{fit}$. At this stage, as can be seen from figures 4.3, and4.4, the error of the magnitudes and colors estimations is unacceptably high for some of the simulated images; therefore, I investigated the other parameters that might affect the goodness of the light model fits.
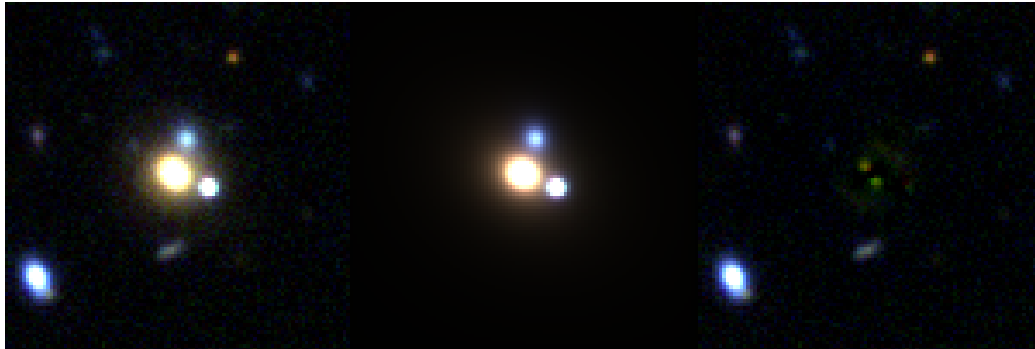
4.3   Contaminating Objects

Figure 4.5: *Left: a typical simulated lens-source system, suffering from the contaminating light of an extra galaxy, too close to the system; int this case the white galaxy, to the bottom-right of the source is an galaxy not belonging to source or lens plane. Middle: 3 Sersic light models have been fitted to the 3 galaxies. Right: residuals; eliminating the best fit light models for the 3 objects from the simulated image. These images are the combination of all 5 grizy bands, and and the dimensions are 16.8″x16.8″.*

As mentioned in 4.2, to minimize the light contamination from the surface brightness of the galaxies other than deflector and source during the light model fit, extra objects have been masked by using the SExtractor, which is handling the task very well when the separation and the surface brightness ratios are enough to consider the object as separate ones; but when the separation is not enough and the extra object is too close to lens or source, SExtractor would not consider them as separate objects, result them not being identified individually, and hence not getting masked; this would be specially the case in the presence of a satellite galaxy at the lens plane. One solution would be to mask these extra leftovers manually, after running the SExtractor, which would not be always possible; it might not always be possible to define a boundary between the extra object and the lens-source system, because there exists no scenario in which you do not lose major parts of the lens or source surface brightness, and hence affecting their real light model shape drastically by using the mask. In such cases, the reasonable approach would be fitting another Sersic profile to that extra object(s), which will make the calculations heavier, but results a descent approximation to the multi-band magnitudes of the lens-source system, and the extra object(s); this is what I have done whenever such a thing happened.

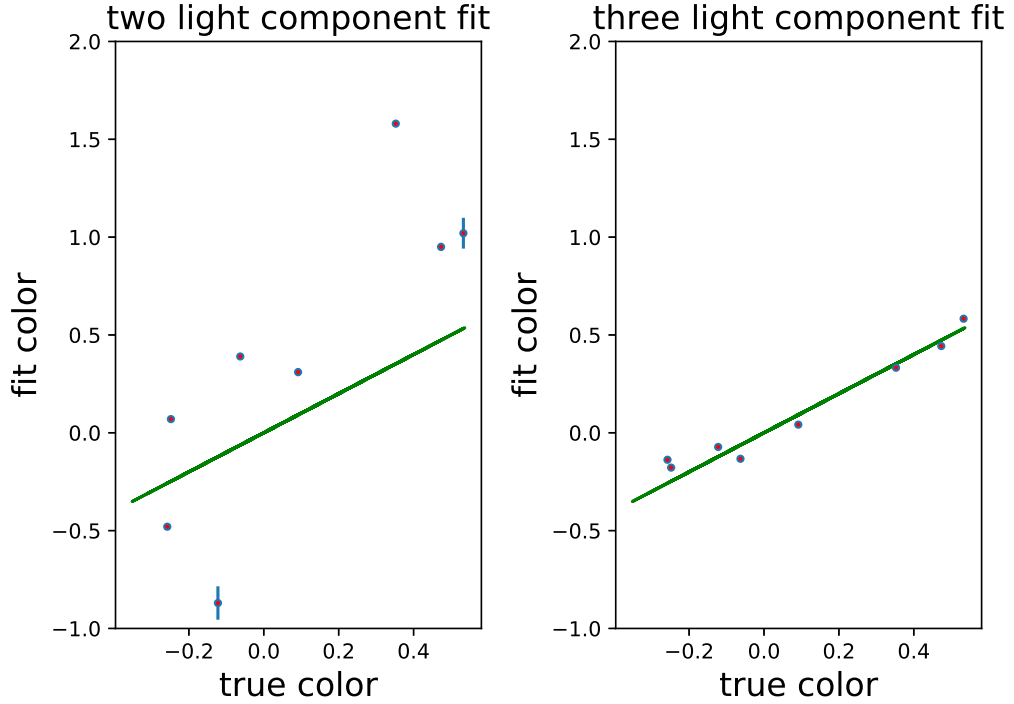Among the population of 60 simulated lens-source system used in sec-

Figure 4.6: *Fitted color vs true color. Left: 8 cases from the previous 60 simulated lens-source systems, in which an extra galaxy too close to the system exists, and the fit could have improved by adding a third light model to account for the contaminating objects. Right: improved fit. Color is defined as the g-band magnitude minus i-band magnitude, and for green line $C^{fit} = C^{true}$.*

tion 4.1, there were 8 cases, whom were still suffering from the light of contaminating objects after using the masks produced via SExtractor, or manually; in each case, after achieving a best possible fit with fitting two light models of the section 4.2, a third Sersic light model has been introduced, positioned at the central pixel of the contaminating object. First by fixing the lens and source models, an approximate fit has been achieved, which has been used as a starting point to fit all the three models together at the next step. A typical 3-light model fit to a case suffering from contaminating objects, too close to the lens-source system, can be seen in figure 4.5; figure [8contaminationobjects] shows the comparison between estimated colors and true colors for these cases. The standard deviations $\sigma(\delta m_\alpha / m_\alpha)$ for 5 *grizy* bands were (0.06,0.08,10,0.14,0.14) respectively, and the standard deviation for color $\sigma(\delta C/C)$is equal to 0.07)

4.4 Lens to Source Surface Brightness Ratio

As I said before, one of the main reasons for choosing the methods of this section (fitting the light models), is to handle the source surface brightness complications raising because of the lens. Here the correlation between the lens to source relative surface brightness, and the goodness of the fits, would be investigate. These will include, effects of the lens being too bright compared to the source, or the source being too close to the center of the lens.
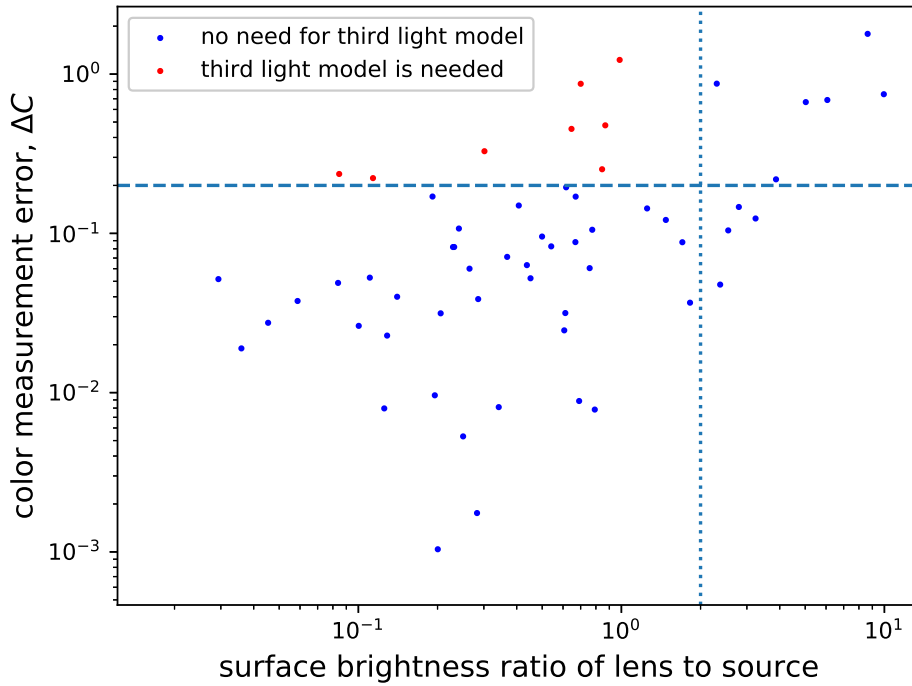

Figure 4.7: *color measurement errors absolute value vs surface brightness ratio of the lens to source at the source position, the horizontal line shows the cutoff for 0.2 error on color ($\delta C > 0.15$), and the vertical line is specifying the surface brightness ratio cutoff (2.0), after which, measurements with errors color errors bigger than 0.15, will be unreliable.*

I defined Surface Brightness Ratio $\phi_{L/S}^{\alpha}$, as the ratio of lens to source surface brightness at the source position in photometry band α. For the simulated lens-source systems used in this section, the original lens image (without the added source) is available (section 4.1) in 5 photometry bands, and the source pixel position is known, since it was added upon the

lens at a chosen random (r, θ); hence, it is straightforward to find the pixel value of the lens surface brightness at the source position in each band, from the original lens image I_L^α; moreover, for each band, eliminating the lens image from the simulated lens-source image, produces an image containing only the source, from which it is possible to find the pixel value of the source at its center (source position) I_S^α. Surface brightness ratio $\phi_{L/S}^\alpha$ would be calculated as I_L^α / I_S^α. Figure 4.7 shows the relation between surface brightness ratio in i-band $\phi_{L/S}^i$ and absolute value of the color parameter error (which is defined as $|C^{true} - C^{fit}|$, with color defined as before $C = (m_g - m_i)$, for the same sample of 60 simulated lens-source images as section 4.1.

From the figure 4.7, it is possible to, ignoring the cases for which a third Sersic light model is needed, define a threshold for $\phi_{L/S}^i$ (dotted line in the figure) at 2.0; of the ratio values $\phi_{L/S}^i$ for a case is bigger than this threshold it will highest probability result a wrong color measurement with $\Delta C = |C^{true} - C^{fit}|$ close to 1.0, due to the extreme brightness of the deflector compared to the source, or small angular separations. Since there is no practical way to handle such cases, to measure more reliable magnitudes, it is useful to identify and eliminate them before they participate in the final photometry results; this way, I make sure that if a color has been estimated for a lens-source system it will be reliable with $\Delta C < 0.2$, and those cases whom are suffering from high lens to source ratio will get eliminated before participating in the final results, and the photometric measurements would not result any color estimation for them.

4.5   Lens Residuals

Lens galaxies of the simulated lens-source systems unlike the sources (which are produced via Sersic light model), are real galaxies, and their surface brightness is not completely described by one Sersic light model; therefore, in practice, after the light model fit, there will always remain some residuals (negative or positive) from the lens surface brightness which have not been accounted for by the fitted light profile. To investigate the effects of these residuals on the source photometry, I will use the best fit model to the system (2 components light models fitted to the lens and source); first, to ignore the source for now, I will use the original lens image (the image acquired from the HSC before producing the simulations), and subtract the lens light component of the best fit light model from this image, which would result an image containing the lens residuals. Since the residuals of

the lens at the source position are the ones which would affect the fitted light model to the source, I would define a variable describing these residuals at the source position, as follows; source is described by an elliptical light model, defined by concentric contours on which surface brightness is constant, a margin can be defined by choosing the surface brightness value ($I(R)$,refer to section 4.1) on one of these contours as the threshold and considering all the contours with value above this threshold, belonging to the source, and hence defining a region as the source. I chose the pixel value of the half light radius contour as the threshold, which is,

$$I_{Re}^{\alpha} = I_{max}^{\alpha} exp\left[- \left(2\pi I_{max}^{\alpha} R_e{}^2 n\Gamma(2n)/10^{(27-m_\alpha)/2.5}\right)^{1/2n}\right] \qquad (4.4)$$

in which I_{max}^{α} is the maximum pixel value of the source in α-band, R_e the half light radius, I_{Re}^{α} pixel value at the half light radius for band α, n the Sersic index, and m_α the magnitude. I_{Re}^{α} can be derived for each one of the photometry bands, using the respective magnitude m_α and I_{max}^{α}; this limits the source within a well defined elliptical region for each one of the bands.

From the residuals image, every pixel which belongs within these margins, can be considered as the lens residual at source position; by defining the residuals ratio ψ_α in band α as,

$$\psi_\alpha = \frac{\Sigma(\text{pixel values of the residuals within the source margins, in band } \alpha)}{\Sigma(\text{pixel values of the source within the source margins, in band } \alpha)},$$
$$(4.5)$$

performing the same practice for the images of the lens residual, and source, in the g and i bands, results the residual ratios in both bands, ψ_g, ψ_i. It can be derived that the source color estimation error ΔC, depends on ψ_g, ψ_i as follows; color C is defined as $m_i - m_g$, hence, using equations 4.2 and 4.3, knowing that R_e is the same for two bands of the same source (section 4.2),

$$C = 2.5(\log I_0^i - \log I_0^g). \qquad (4.6)$$

Effects of adding the extra surface brightness δI^i, and δI^g to the I_0^i and I_0^g respectively, on the color C would be,

$$C' = 2.5\left[\log(I_0^i + \delta I^i) - \log(I_0^g + \delta I^g)\right]; \qquad (4.7)$$

subtracting C from C'results the δC as,

$$\delta C = 2.5\left[\log(1 + \frac{\delta I^i}{I_0^i}) - \log(1 + \frac{\delta I^g}{I_0^g})\right]; \qquad (4.8)$$
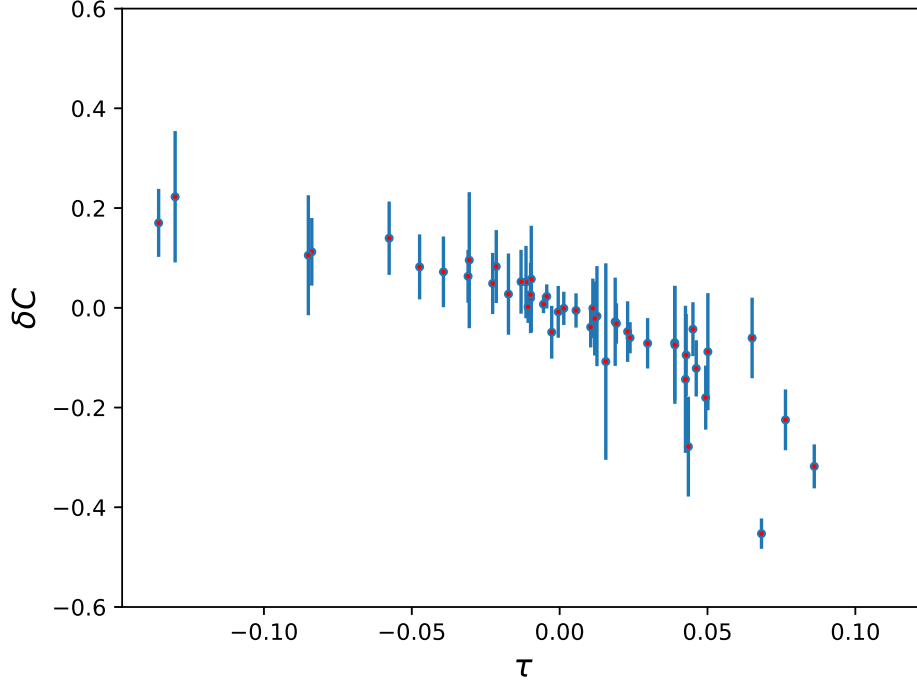
Figure 4.8: *Color error δC dependence on the τ value defined in equation 4.8. This includes 46 simulated lens-source systems from section 4.2, which are not suffering from high surface brightness, or contaminating objects.*

since $\delta I^i / I_0^i$ and $\delta I^g / I_0^g$ are nothing but the ψ_i, ψ_g defined in equation 4.5, δC can be rewritten as,

$$\delta C = 2.5 \left[\log(1 + \psi_i) - \log(1 + \psi_g) \right]; \tag{4.9}$$

hence, it is useful to define τ as,

$$\tau = log(\frac{1 + \psi_i}{1 + \psi_g}). \tag{4.10}$$

Figure4.8 shows the color error δC versus τ, for the 60 simulated lens-source systems of section 4.2.

It can be seen from 4.8, that there is a linear relation between δC and τ as was expected from equation 4.9; lens divergence from an elliptical light model will affect the goodness of the fit, and the accuracy of color and

magnitudes. One way to identify the cases for which this effect in would cause unreliable photometry, in practice, would be subtracting the best fit lens and source models from the image, and examining the lens residuals; if the lens residuals are big everywhere but close to the source, it means that the source model has been accounting for the lens residuals at source position, resulting unreliable source photometry.

Chapter 5

Testing the Algorithm

In the previous chapter, simulated sources were produced by choosing their spectral energy distributions (SED) from the template libraries, and, by fitting a Sersic profile, magnitudes of each source in 5 photometry bands (*grizy*), were measured. In this chapter, using the same method to produced the simulation, the photo-z estimator of section 3.2 will be employed to estimate the redshift, and its outlier fraction 3.7.

As discussed before (sections 4.3,4.4,4.5), accuracy of the magnitude measurements depends on various factors, including the shape of the lens, surface brightness ratio, and contaminating objects; furthermore, as was also the case in figure 4.3, the magnitude measurement uncertainty depend on the photometry band, growing from g to y. From section 4.2, a typical uncertainty for each band can be approximated; using these uncertainties as the observer uncertainties for the photo-z estimator, the redshift of the source can be estimated.

It has been showed in chapter 4, that for cases in which surface brightness ratio is higher than 2, color estimation becomes unreliable with typical errors (ΔC) above 0.20 (corresponding to a Gaussian uncertainty of at least 0.20 on each one of the i and g bands); as shown in figure 3.2, photo-z estimation using such erroneous photometry, would result an outlier fraction above 35%. By flagging systems with surface brightness ratios above 2, their photometric redshift will not be estimated, as a step toward more reliable photo-z. One might argue that in this practice, since by producing the simulations, surface brightness ratio is straightforward to calculate (section 4.4), flagging the source with high surface brightness ratio would be unrealistic, and not practical for real observations; even though it would not be possible to completely separate the surface brightness of the source and lens for a real strongly lensed system, by using the best light
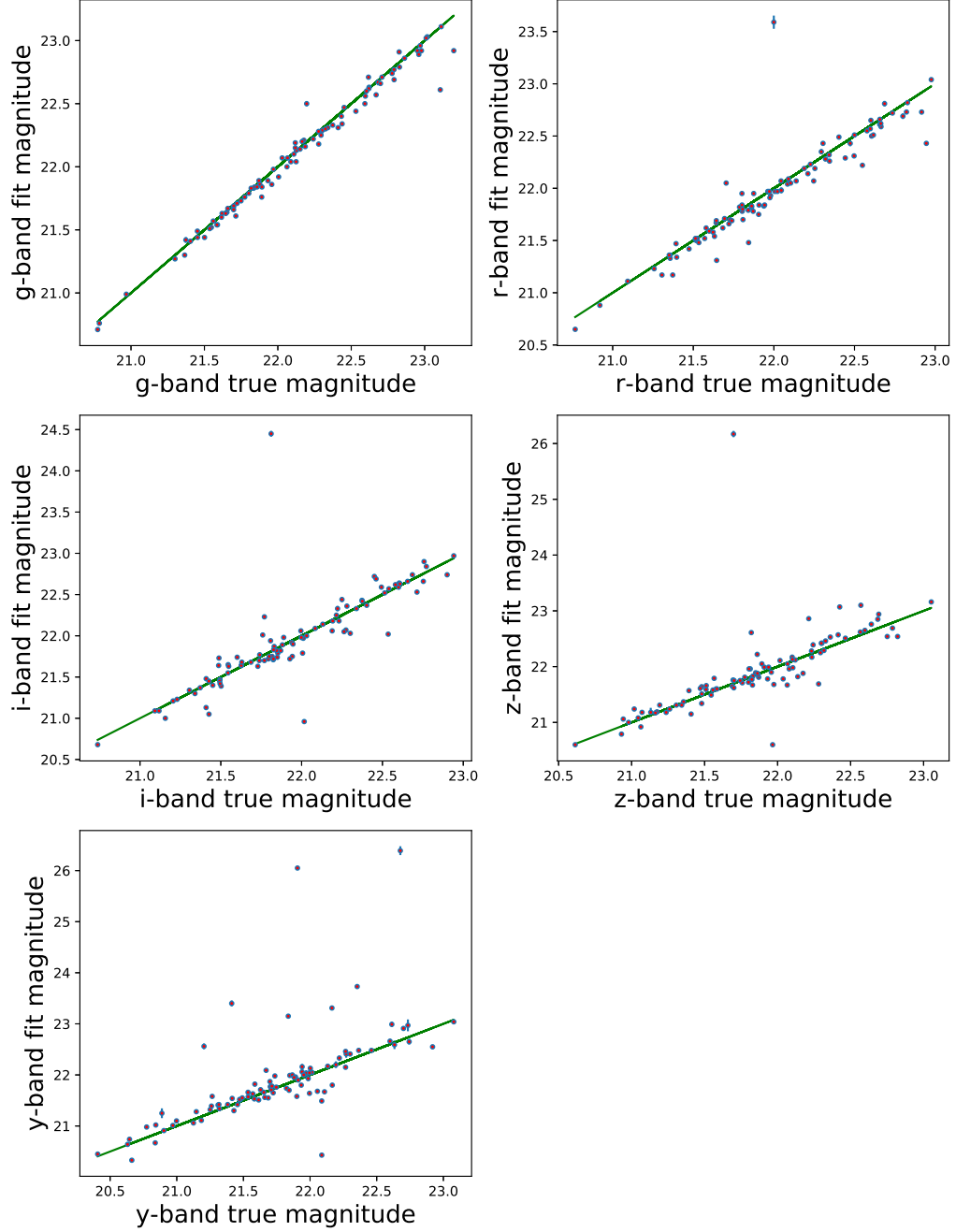
33

Figure 5.1: *Multi-band photometry for 100 simulated lens-source systems; an automatic script was used to fit the light models. Green line is the $m^{true} = m^{fit}$ line.*

model fits to the source and deflector, the order of magnitude of surface brightness ratio can be approximated.
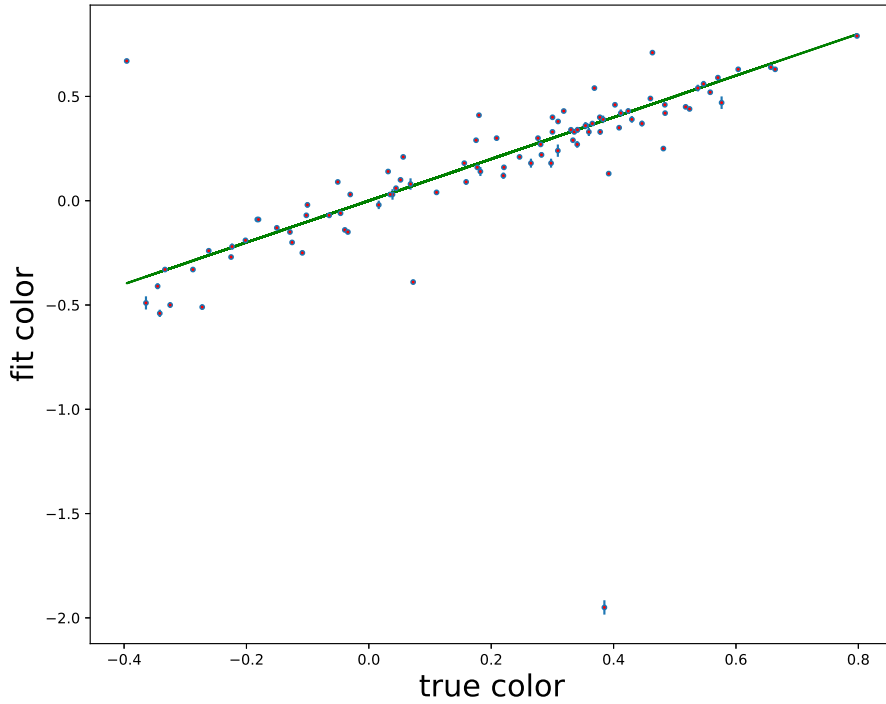

Figure 5.2: *The fitted colors to the same 100 simulated lens-source systems of figure 5.1. Green line shows the ‚true color = fit color‚ line.*

After producing a sample of 100 simulated lens-source systems (following the methods of section 4.1), I used a script to flag the objects with high surface brightness ratios, and fit the two-component Sersic light profiles to the remaining 93 lens-source systems. Inputs were *grizy* 100x100 pixel simulated lens-source images, point spread functions for each band, and variance maps. For the light model fit to the source, similar to section 4.2, elliptical light model parameters have been limited around their true values as follows; source position within ± 2.5 pixels in each one of the x and y directions, orientation within ± 2.5 degrees, and ± 0.1 for Sersic index, axis ratio, and half light radius. The measured 5-band magnitudes and colors for the source can be seen in figures 5.1, and 5.2. These five-band magnitudes and their respective uncertainties, has been used to run the photo-z algorithm of chapter 2; the PDF, and maximum likelihood red-
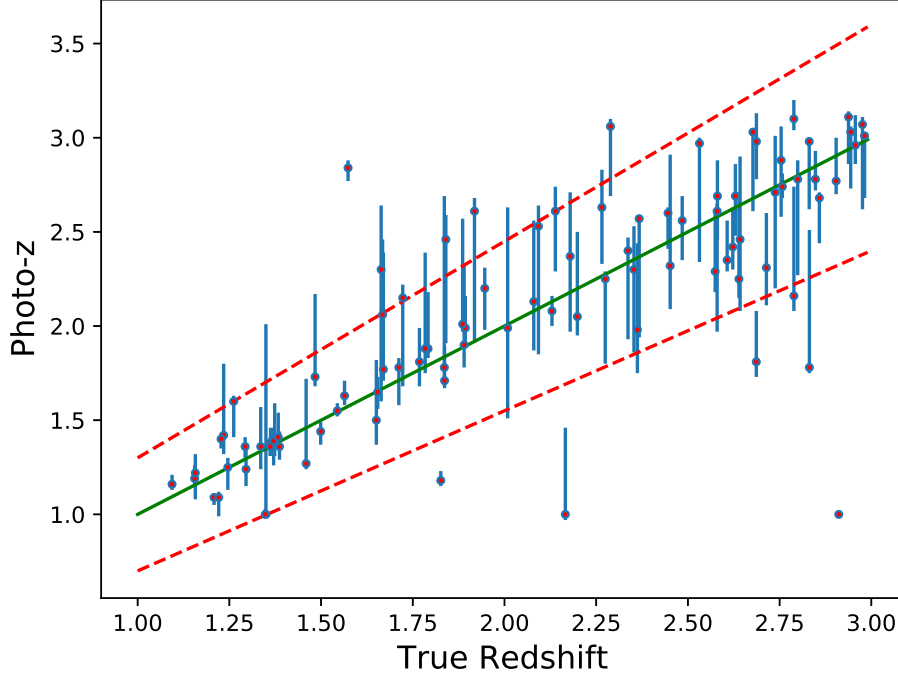
Figure 5.3: *estimated photo-z vs true redshift, using the automatic algorithm, on a sample of 100 simulations of lens-source systems, with measured magnitudes of figures 5.1, and 5.2. The Green lines is the photo-z = true redshift, line, red-dashed lines are specifying the region in which the standard deviation is smaller than 0.15 ($\sigma(\delta z_{phot}/1+z) < 0.15$), and the error bars are showing the 68 percentile of the redshift PDF for each case.*

shift, have been estimated for each one of the sources. Results can be seen in figure 5.3, showing the source photometric redshift estimation versus the true redshift; the blue solid line is the equality lien (photo-z = true redshift), and the dashed lines specify the region in which $\Delta z/(1+z) < 0.15$. Uncertainty bars on each one of the scatter points of this figure are calculated as the first sigma standard deviation of the PDF. The outlier fraction (equation 3.7) of the estimated photometric redshifts is 13.9%, with 0.08 standard deviation ($\sigma(\Delta z/1+z_{phot})$).

Chapter 6

Discussion

Studying simulated lens-source systems (defined in section 4.1, adding a simulated elliptical source on top of a real lens), by fitting Sersic surface brightness profiles to the lens and source, I was able to evaluate galaxy (source and deflector) magnitudes in HSC *grizy* photometry broad bands. The magnitude measurements of the source are reliable enough (with *i*-band standard deviation of 0.10) to perform precise photometric redshift estimations with 13.9% outlier fraction.

6.1   Fitting the Light Components

In chapter 4, I showed that the goodness of the light model fit to lens-source systems, depends most importantly on the surface rightness ratio of lens to source, as expected. This is simply equal to the following statement; if the lens is too bright compared to source, it might totally dominate the overall surface brightness of the system, causing the source surface brightness to become hard to detect. In fact, extreme scenarios (with surface brightness value above 5.0), cause the source surface brightness to look like a fluctuation in that of lens. Nevertheless, some of these cases could be misleading, since due to lack of required angular resolution they would not be selected as strongly lensed systems at the first place; therefore, when it comes to a practical study of real strongly lensed systems, they would rarely participate in our samples. Although, it is inevitable that by further developments on selection algorithms, and survey angular resolutions, this ratio limit for detected strong lensing systems will eventually grow; but, it would be useful to know the limitations of this method before implementation for redshift estimations. As showed in section 4.3,

37

a good cutoff value for surface brightness ratio ratio is 2.0; by continuously checking and filtering the objects for which the surface brightness ratio is higher than this, we can make sure of the accuracy of the estimated photometric redshifts. Moreover, due to the nature of the simulations of this paper, involving the use of random lens galaxies, many of the high surface brightness ratios happened as a result of source being placed on the lens, which has relatively lower probability to happen in reality. It would be straightforward to modify the algorithm responsible for producing the simulations, to produce more realistic scenarios; by first approximating the lens galaxy surface brightness, and avoiding placing the sources in high surface brightness regions. Obviously this requires a detailed consideration of strong lensing theory to avoid production of systematic biases.

Nevertheless, simplest approach would be ignoring high surface brightness scenarios for now, since it would not be possible to estimate an accurate photo-z based on them. This is what has been done, when testing the performance in chapter 5; as also discussed there, we are in need of an algorithm to calculate this ratio as precise as possible in a practical manner, applicable to general strongly lensed systems. It may involve fitting the lens and source as good as possible and using the fitted Sersic profiles to approximate the ratio; but there is much progress to be made in order to estimate it precisely.

Moreover, there has been many cases, in which the existence of satellites or other secondary objects not belonging to the lens plane, affected the goodness of the fit; I should add that, such scenarios have a slight probability to happen. However, in case of happening, this would be relatively easy to handle, by either introducing extra light models to account for the unrelated objects (secondary objects other than lens and source), or using masks to ignore the regions in which their surface brightness dominates (sections 4.2,and 4.3). The automated version of the algorithm, achieving the results of chapter 5, has used masking to handle such cases; but, experience shows that, there can be objects, specially satellites belonging to the lens plane, which would not get recognized as separate objects, at least using Source Extractor; it would be practical to modify the algorithm to flag such cases (when the extra object is not getting masked out) whenever happening.

Sersic profile is not always a good approximation to the lens surface brightness; in my opinion this is the major challenge raising whenever implementing the algorithm of this paper. As seen in chapter 4, cases with $\tau > 0.05$, which would still get flagged as strongly lensed systems with current selection algorithms, will result inaccurate color measurements with typical color errors bigger 0.1; as seen in chapter 3, using such in-

accurate color measurements would result photo-z estimations with outlier fractions bigger than 40 percent. Suggestions to handle such situations would be regularly weighting lens residuals during the fitting process, flagging the drastically troubled systems with τ values bigger than 0.1, eliminating best fit lens model from the image for such flagged systems, and search for asymmetries in source plus lens-residual image. By assuming the source to have elliptical symmetric axes, we can minimize the aforementioned asymmetries, and perform a more accurate color, and consequently photo-z estimation.

6.2 Photo-Z Performance

The simple photo-z estimation algorithm developed in chapter 2, containing no prior information (in contrast to for example BPZ, Benítez, 2000), was employed to estimate the redshift for equally easy scenarios; source galaxies have been simulated by selecting their spectral energy distributions (SED) from the same templates (redshift-color space) that were used to estimate the probability distribution function (PDF) and maximum likelihood redshifts. For such simulated source galaxies, if the magnitude estimations are precise enough (with small uncertainties, typically in orders smaller than 0.03 for the magnitude of each band, as shown is chapter 2), photo-z algorithm will result the true redshifts (within the redshift resolution used to run the it), with outlier fractions smaller than 1%. The uncertainty on magnitude measurements depend on previously mentioned (section 6.1) complications caused by lens surface brightness; for the simulated lens-source systems tested in chapter 5, I showed the uncertainty on the estimated *i*-band magnitudes, excluding sources with surface brightness ratio bigger than 2.0 (for reasons discussed at 6.1), to be 0.1 with $\sigma(\Delta z_{phot}/(1 + z_{phot})) \propto 0.80$, and 13.9% respective photo-z outlier fraction, which can get improved significantly by accounting for the points mentioned in 6.1.

As a comparison of these results with a general survey photometry, I should mention (Tanaka et al., 2018) whom, by estimating photometric redshifts based on HSC five-band photometry, concluded that their results are most accurate in redshift range 0.2 to 1.5, achieved 8% outlier fraction for bright galaxies, and $\sigma(\Delta z_{phot}/(1 + z_{phot})) \propto 0.04$, with *i*-band magnitudes smaller than 24. Despite the complications caused by surface brightness of deflector, the algorithm developed throughout this paper was able to perform photo-z estimation for simulated source, with comparable accuracy to that of best photo-z measurements ever performed; hence it is

worthwhile to further investigate the concept.

Furthermore, the uncertainty values for magnitude of each band, used as as input for the photo-z algorithm, is of critical importance; this value being drastically wrong for any of the photometry bands will result the PDF becoming either very broad, with no practical scientific use (as it will contain a very large range of redshift within the 68 percentile, hence limiting the redshift to no specific region), or very narrow with a drastically wrong peak as the photo-z estimation (in such cases it is in general more useful to have a wider PDF including the true redshift value); therefore, it becomes important to calculate the magnitude uncertainties carefully, and case by case.

As mentioned earlier, for simulated sources of this paper, having the same SED as those of template members, it is relatively easier to estimate the photo-z, compared to real scenarios; although this justifies the usage of the simple maximum likelihood photo-z algorithm, developed in chapter 3, in practice, to repeat the same method of this paper on real strongly lensed objects, it will be essential to employ advanced photo-z algorithms to achieve satisfactory results; (Benítez, 2000; Bolzonella et al., 2000; Tanaka et al., 2018).

6.3   Future Plan

This algorithm is still in the earliest stages of development, and there is much to be done to increase the performance. As mentioned earlier in this chapter, many intrinsic algorithms need to get developed in terms of identifying the objects for which it would not be wise to use this method; for example, improvements on the issues discussed in the first part of this chapter, will be important to increase the reliability.

Moreover, this algorithm needs to get tested (and modified respectively) on three new test samples; each one of the following cases will require a similar treatment to that of this paper, with slight adjustments. First case, will be producing the same set of simulations (non-lensed source galaxies), but instead with real source galaxies added on top of the lenses; this will need a more advanced photo-z estimator, ideally, using prior information to estimate the redshift, similar to BPZ (Benítez, 2000). Second case should be adding strongly lensed features to simulated surface brightness of the source, by assuming a mass model for the deflector. Deriving the Lensing Jacobian, using the defined mass profile of deflector, will make us able to produce a strongly lensed image of a simulated source; adding this new source on top of the lens will produce the simu-

lated strongly lensed systems. Fitting a Sersic surface brightness profile to these simulated images, requires a mass estimation for the deflector at the same time; to fit the surface brightness the source, first, an elliptical light model is produced using Sersic model(same as what was done during this paper), which then gets deflected by a mass estimation of the lens galaxy. At the end, the algorithm should be tested on real images of strongly lensed galaxies.

As was validated in chapter 5, this algorithm can perform with minimum human interventions, measuring the multi-band magnitudes of the provided simulated lens-source images, and estimating the photo-z based on them. This can become extremely useful in the near future, when the availability of tens of thousands of strongly lensed systems will make the individual study of all of them impossible. Using such algorithms would give us the ability to estimate the source redshift for the whole population in a timely, efficient manner, which, alongside the redshift of the source, can be used to estimate the the critical density of the deflector and the mass inside Einstein Radius. This in fact has the potential to, be employed in IMF, and dark matter fraction studies of a wide range of redshifts for massive early-type deflectors.

Chapter 7

Conclusion

Strongly lensed galaxy-galaxy systems, by measuring the total mass inside Einstein Radius, proved to be one of the best tools to study stellar initial mass function (IMF), and dark matter fraction inside inside that radius; their significance becomes hardly deniable in high redshift studies, for which due to paucity of mass tracers at large radii (where the dark matter dominates), dark matter investigations can not rely on galaxy dynamics.

Nevertheless, inferring the source redshift, is remained the major challenge in calculating Critical Density and the mass inside Einstein Radius for the faint sources of discovered strongly lensed systems. Using spectroscopy is expensive and is not always guaranteed to be successful; on the other hand, the enormous sample of such systems about to become available, completely rules out the possibility of achieving spectroscopic redshifts for all of them.

Photometric redshift estimation (photo-z), with first sigma standard deviations $\sigma(\Delta z / 1 + z_{spec})$ of orders of 5~10 percent for large galaxy surveys, provides a faster/cheaper alternative to spectroscopy, specially for faint objects, and therefore raising as a method worth investigating. Whenever attempting photometry for strongly lensed systems, source surface brightness complications due to the dominant lens light, is going to raise as the main technical difficulty.

Using a simplified test sample, constructed by adding elliptical light profiles, produced via choosing the spectral energy distributions (SED) from empirical/population synthesis redshift-color templates, as sources, on top of the real images of massive early-type galaxies as defectors in 5-band photometry of HSC survey (*grizy*), I verified that by assuming Sersic light profiles for the source and deflector, we can describe the overall

43

surface brightness of such system, with reliable magnitude measurements $\sigma(\Delta m/m) = 0.10$. I calculated the photometric redshifts of the sample, based on the measured magnitudes and achieved accurate photo-z(s) with $\sigma(\Delta z/1 + z_{ref}) = 0.08$, and 13.9 percent outlier fraction.

These results, in terms of accuracy, are comparable to those of large galaxy survey photometry, approving the potential of the method developed throughout this paper. I also found the goodness of the fit (and hence, photo-z estimation), to be an increasing function of most importantly lens to source surface brightness ratios, divergence of the deflector surface brightness from an elliptical Sersic profile, and contaminating surface brightness of the secondary objects other than the lensing system; some intrinsic scripts have been added to the main algorithm to modify the fit, accounting for the aforementioned parameters, or exclude the case from the photo-z estimations whenever the outcome has been predicted to be unreliable (7% of the total test objects were excluded automatically due to this). This way, I made sure that if we estimate a redshift, it is going to be reliable, and the troubled cases are going to get flagged before participating in the final results.

Due to the mild dependency of strong lensing critical density on source redshift, achieved accuracy of this paper would be sufficient to limit the critical mass of massive early type galaxies. Although, a practical implementation of this algorithm, requires further modifications and developments by performing the same practice on more realistic samples.

This algorithm has also been developed to be fully functional automatically, without the requirement of human interactions throughout light model fitting, outlier flagging (predicting the objects for which the photometry is going to be unreliable), and redshift estimating. This types pf algorithms have the potential to address the problem of redshift estimation for the numerous upcoming strong lensing systems.

Acknowledgments

I would like to express my sincere gratitude toward my both supervisors, Prof. Henk Hoekstra, and Dr. Alessandro Sonnenfeld, who helped me stay on the right path, and made this research possible through their wise guidance. I like to specially thank Alessandro, who was always available, and spent enormous time and effort to train me as a true research.

References

2006, Gravitational Lensing: Strong, Weak and Micro (`arXiv:astro-ph/0407232`)

Aihara H., et al., 2018, PASJ, 70, S8

Auger M. W., Treu T., Bolton A. S., Gavazzi R., Koopmans L. V. E., Marshall P. J., Moustakas L. A., Burles S., 2010, ApJ, 724, 511

Barnabè M., Czoske O., Koopmans L. V. E., Treu T., Bolton A. S., 2011, MNRAS, 415, 2215

Benítez N., 2000, ApJ, 536, 571

Bertin E., Arnouts S., 1996, A&AS, 117, 393

Bertin G., Stiavelli M., 1993, Reports on Progress in Physics, 56, 493

Bolton A. S., Burles S., Koopmans L. V. E., Treu T., Moustakas L. A., 2006, ApJ, 638, 703

Bolton A. S., Burles S., Koopmans L. V. E., Treu T., Gavazzi R., Moustakas L. A., Wayth R., Schlegel D. J., 2008, ApJ, 682, 964

Bolzonella M., Miralles J. M., Pelló R., 2000, A&A, 363, 476

Brault F., Gavazzi R., 2015, A&A, 577, A85

Brownstein J. R., et al., 2012, ApJ, 744, 41

Bruzual G., Charlot S., 2003, MNRAS, 344, 1000

Cabanac R. A., et al., 2007, A&A, 461, 813

Carrasco Kind M., Brunner R. J., 2013, MNRAS, 432, 1483

Ciotti L., Bertin G., 1999, A&A, 352, 447

Cole S., Lacey C. G., Baugh C. M., Frenk C. S., 2000, MNRAS, 319, 168

Coleman G. D., Wu C. C., Weedman D. W., 1980, ApJS, 43, 393

Collett T. E., 2015, ApJ, 811, 20

Collett T. E., Auger M. W., 2014, MNRAS, 443, 969

Connolly A. J., Csabai I., Szalay A. S., Koo D. C., Kron R. G., Munn J. A., 1995, AJ, 110, 2655

Davis M., Efstathiou G., Frenk C. S., White S. D. M., 1985, ApJ, 292, 371

Dawson K. S., et al., 2013, AJ, 145, 10

Diehl H. T., et al., 2017, ApJS, 232, 15

Gavazzi R., Marshall P. J., Treu T., Sonnenfeld A., 2014, ApJ, 785, 144

Hernquist L., 1990, ApJ, 356, 359

Inada N., et al., 2012, AJ, 143, 119

Ivezić Ž., et al., 2019, ApJ, 873, 111

Kassiola A., Kovner I., 1993, ApJ, 417, 450

Kinney A. L., Calzetti D., Bohlin R. C., McQuade K., Storchi-Bergmann T., Schmitt H. R., 1996, ApJ, 467, 38

Komatsu E., et al., 2009, ApJS, 180, 330

Komatsu E., et al., 2011, ApJS, 192, 18

Koo D. C., 1985, AJ, 90, 418

Kormann R., Schneider P., Bartelmann M., 1994, A&A, 284, 285

Kuhlen M., Keeton C. R., Madau P., 2004, ApJ, 601, 104

Kuijken K., 2003, arXiv e-prints, pp astro–ph/0304438

Kuijken K., et al., 2015, MNRAS, 454, 3500

Laureijs R., et al., 2011, arXiv e-prints, p. arXiv:1110.3193

Madau P., 1995, ApJ, 441, 18

Meneghetti M., Bartelmann M., Moscardini L., 2003, MNRAS, 340, 105

Narayan R., Bartelmann M., 1996, arXiv e-prints, pp astro–ph/9606001

Navarro J. F., Frenk C. S., White S. D. M., 1996, ApJ, 462, 563

Navarro J. F., Frenk C. S., White S. D. M., 1997, ApJ, 490, 493

Peebles P. J. E., 1980, The large-scale structure of the universe

Planck Collaboration et al., 2018a, arXiv e-prints, p. arXiv:1807.06205

Planck Collaboration et al., 2018b, arXiv e-prints, p. arXiv:1807.06209

Ruff A. J., Gavazzi R., Marshall P. J., Treu T., Auger M. W., Brault F., 2011, ApJ, 727, 96

Salpeter E. E., 1955, ApJ, 121, 161

Sawicki M. J., Lin H., Yee H. K. C., 1997, AJ, 113, 1

Schaye J., et al., 2015, MNRAS, 446, 521

Schlegel D., White M., Eisenstein D., 2009, in astro2010: The Astronomy and Astrophysics Decadal Survey. p. 314 (arXiv:0902.4680)

Sersic J. L., 1968, Atlas de Galaxias Australes

Sonnenfeld A., Treu T., Gavazzi R., Marshall P. J., Auger M. W., Suyu S. H., Koopmans L. V. E., Bolton A. S., 2012, ApJ, 752, 163

Sonnenfeld A., Treu T., Gavazzi R., Suyu S. H., Marshall P. J., Auger M. W., Nipoti C., 2013, ApJ, 777, 98

Sonnenfeld A., Wang W., Bahcall N., 2019, A&A, 622, A30

Suyu S. H., et al., 2014, ApJL, 788, L35

Tanaka M., et al., 2018, PASJ, 70, S9

Treu T., 2010, ARA&A, 48, 87

White S. D. M., Rees M. J., 1978, MNRAS, 183, 341